metals

MDPI

Article

The Al Effects of Co-Free and V-Containing High-Entropy Alloys

Songqin Xia [1], Xiao Yang [1,2,*], Mingbiao Chen [3], Tengfei Yang [4] and Yong Zhang [1,*]

1 State Key Laboratory for Advanced Metals and Materials, University of Science and Technology Beijing, Beijing 100083, China; xsq2417@163.com
2 State Key Laboratory for Advanced Metallurgy, University of Science and Technology Beijing, Beijing 100083, China
3 College of Mechanical Engineering, Qinghai University, Xining 810016, China; chenmingbiaozyx@126.com
4 State Key Laboratory of Nuclear Physics and Technology, Center for Applied Physics and Technology, Peking University, Beijing 100871, China; tyang@utk.edu
* Correspondence: yangxiao_sky@163.com (X.Y.); drzhangy@ustb.edu.cn (Y.Z.); Tel.: +86-10-6233-3073 (Y.Z.)

Academic Editor: Vincent Fournée
Received: 19 December 2016; Accepted: 5 January 2017; Published: 10 January 2017

Abstract: In this study, five-component high-entropy alloys (HEAs) Al_xCrFeNiV (where x denotes the molar ratio, x = 0, 0.1, 0.3, 0.5, 0.75, 1, and 1.5) were prepared using an arc-melting furnace. The effects of the addition of the Al on the crystal structures were investigated using X-ray diffraction (XRD), scanning electron microscopy (SEM), and transmission electron microscopy (TEM). Also, two non-equiatomic ratio HEAs, Al_xCrFeNiV (x = 0.3, and 0.5), were systematically studied through the use of various characterization methods in the as-cast state. The $Al_{0.3}$CrFeNiV alloy displayed typical duplex body-centered cubic (BCC) structures, including disordered BCC (A2), and NiAl-type ordered BCC (B2) phases. Meanwhile, in regard to the $Al_{0.5}$CrFeNiV alloy, this alloy was found to contain an unknown phase which was enriched in Cr and V, as well as the coherent A2/B2 phases. Both of these alloys displayed very high yield and fracture strengths. However, their compression fracture strains were approximately 10%. Also, the fracture surfaces showed mainly cleavage fracture modes.

Keywords: high-entropy alloys; microstructure; compressive properties

1. Introduction

High-entropy alloys (HEAs) are a new class of materials which are defined as alloys consisting of four or more base elements with equal or non-equal fractions. The high configurational entropy which is induced by the number of base elements is able to prevent the formation of intermetallic phases, and thereby avoids the disadvantages of conventional multicomponent alloys. HEAs mainly consist of simple solid solution structures, such as body-centered cubic (BCC), face-centered cubic (FCC), or hexagonal close-packed (HCP) structures [1–3]. However, in many cases, more complicated structures may exist in some HEAs [4–7], including ordered-solid solutions and/or intermetallic phases, which indicates that the high configurational entropy may not be sufficient to prevent the formation of ordered solid solutions and intermetallic phases in some HEAs [8].

Many HEA systems reported are based on transition metals—namely Co, Cr, Fe, and Ni—with the additions of such elements as Al and Mn. The widely studied Al_xCoCrFeNi HEAs are demonstrated from FCC to BCC structures through a mixture of both phases with increased Al content [9]. In recent studies, the HEAs have been reported to exhibit promising irradiation resistance properties, which make them potential cladding material candidates for components of the next-generation nuclear reactors, as well as other high-radiation resistant materials [10–12]. However, considering the

radioactivity of Cobalt in most HEAs under neutron irradiation, exploring these novel HEAs without Co-element is necessary.

In this study, the V-element was added to the widely studied $Al_xCoCrFeNi$ HEAs to replace Co. The two main objectives which were focused on were as follows: (i) To gain new understanding of the Al effects on phase formations in both Co-free and V-containing HEAs; and (ii) To explore the microstructures and mechanical properties of the $Al_xCrFeNiV$ alloys.

2. Experimental Procedures

In this research study, HEAs samples with nominal compositions of $Al_xCrFeNiV$ (where x denotes the molar ratio, x = 0, 0.1, 0.3, 0.5, 0.75, 1, and 1.5) were prepared by the arc-melting of the pure elements in a Ti-gettered high-purity argon atmosphere inside a water-cooled copper mold (SKY Technology Development Co., Ltd. Chinese Academy of Science, Shenyang, China). The purities of the alloying elements were determined to be above 99.95 atomic percent (at %). In order to ensure chemical homogeneity, the ingots were flipped over and re-melted at least five times. The produced ingots of the $Al_xCrFeNiV$ alloys had dimensions of approximately Φ 30 mm × 10 mm. Table 1 lists the composition of the alloys of this work.

Table 1. The composition of the alloys used in the experiment (at %).

Alloy No.	Al	Cr	Fe	Ni	V	Atomic Ratio
1	0	25	25	25	25	CrFeNiV
2	2.4	24.4	24.4	24.4	24.4	$Al_{0.1}CrFeNiV$
3	7.0	23.3	23.3	23.3	23.3	$Al_{0.3}CrFeNiV$
4	11.1	22.2	22.2	22.2	22.2	$Al_{0.5}CrFeNiV$
5	15.8	21.1	21.1	21.1	21.1	$Al_{0.75}CrFeNiV$
6	20	20	20	20	20	$Al_1CrFeNiV$
7	27.3	18.2	18.2	18.2	18.2	$Al_{1.5}CrFeNiV$

The microstructures of the as-cast samples were characterized by XRD (TTRIII, Tokyo, Japan) at 40 kV and 40 mA, with a scanning rate of 2° per minute from 20° to 90°. Then, the prepared samples of Φ 3 mm × 6 mm for the compressive tests were prepared and investigated at room temperature, with a strain rate of 2×10^{-4} per second. Meanwhile, Vickers microhardness, HV, was measured on polished cross-section surfaces of the $Al_xCrFeNiV$ alloys (x = 0.3, 0.5, 0.75, 1, and 1.5) using a 136-degree Vickers diamond pyramid (HV-1000, Shanghai, China) under a 500 g load applied for 15 s. The fracture surface and morphology of the alloys were examined using a scanning electron microscope (SEM, Zeiss Supra 55, Oberkochen, Germany) equipped with an energy-dispersive X-ray (EDX) spectrometer. The transmission electron microscopy (TEM, Technai F30, FEI, Hillsboro, OR, USA)-EDX characterizations were performed under Scanning TEM (STEM) nano-probe conditions, with a beam size of approximately 1 nm. The TEM samples were prepared by mechanical polishing to approximately 40 μm in thickness, followed by the utilization of ion milling. Also, the samples for the SEM/Back Scattered Electron (BSE) study were prepared by electro-polishing at room temperature, in a solution of $HClO_4$ (15%), CH_3OH (60%), and $CH_3(CH_2)_3OH$ (25%).

3. Results

3.1. Results of the XRD and SEM

Figure 1a shows the XRD patterns of the $Al_xCrFeNiV$ HEAs, and Figure 1b shows the macroscopic samples of the three representative alloys, including CrFeNiV, $Al_{0.3}CrFeNiV$, and AlCrFeNiV, respectively. The crystal structures of those alloys with lower Al content (for example, x = 0 and 0.1) were quite different from that for the alloys with higher Al content (for example, $x \geq 0.3$). For CrFeNiV alloy, the diffraction patterns might be identified with FCC or $L1_2$ structure. Meanwhile, with regard

to the $Al_{0.1}$CrFeNiV alloy, an FCC solid solution and a BCC solid solution coexisted in the alloy, but there were still some unidentified peaks for the two lower Al content alloys. For the x = 0.3, all of the diffraction patterns could be identified with typical duplex BCC structures, including the A2 and B2 phases. For $x \geq 0.5$, along with the similar duplex BCC structures, there were minor unidentified peaks at small 2θ angles, which corresponded to an 'unknown phase' in the present study. These results confirmed that the increase of Al content could affect the structures of the Al_xCrFeNiV alloys. The representative macroscopic features of the as-cast ingots are shown in Figure 1b. Both the $Al_{0.1}$CrFeNiV and CrFeNiV alloys broke into many pieces immediately following the arc-melting. The alloys of the $Al_{0.75}$CrFeNiV, AlCrFeNiV, and $Al_{1.5}$CrFeNiV broke into two pieces. In contrast, the as-cast ingots of the $Al_{0.3}$CrFeNiV and $Al_{0.5}$CrFeNiV samples did not break (as shown in Figure 1b), which might have indicated a better ductility. Their microstructure and mechanical properties were also further investigated in this present study.

The SEM/BSE images of the $Al_{0.3}$CrFeNiV and $Al_{0.5}$CrFeNiV HEAs are shown in Figure 2. A large number of nano-precipitations were commonly observed in the $Al_{0.3}$VCrFeNi alloy. The XRD and SEM results verified that the $Al_{0.3}$CrFeNiV alloy was one of the typical duplex BCC structures with A2 and B2 phases. The $Al_{0.5}$CrFeNiV (Figure 2b) presented a more complicated microstructure, with a periodic fine-scale (approximately 100 nm in width) structure consisting of obvious alternating bright and dark interconnected phases. These were found to be similar to the inter-dendritic and inter-plate region structures in the selected Al_xCoCrFeNi alloys [13], which were believed to have been formed by a spinodal decomposition mechanism [14]. Similar structures were also reported in the Al_xCoCrCuFeNi [15] and AlFeMnNi HEAs [16]. In order to further confirm the microstructures of both the HEAs, TEM and STEM analyses were performed in this research study.

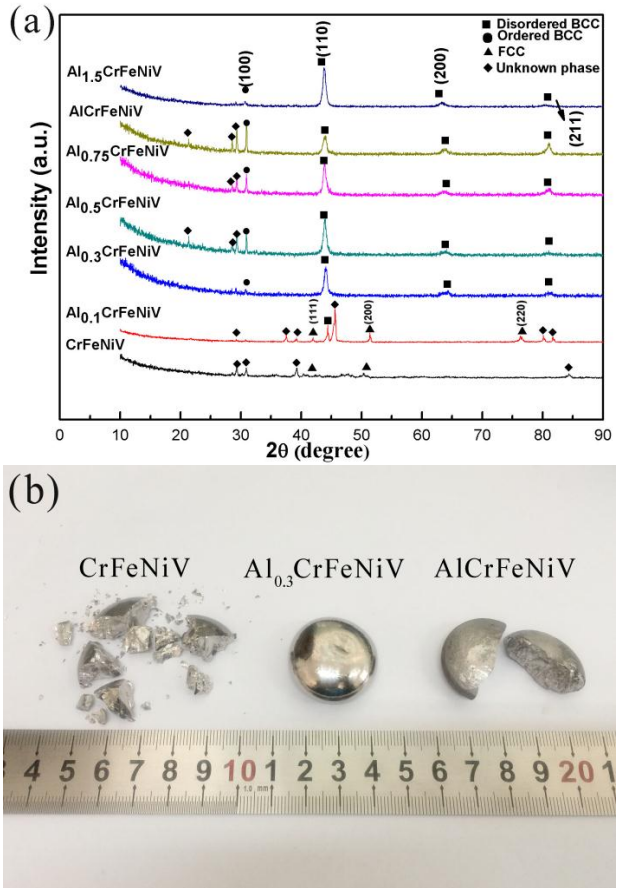

Figure 1. (**a**) XRD patterns of the as-cast Al_xCrFeNiV HEAs; (**b**) Macroscopic samples of the three representative alloys CrFeNiV, $Al_{0.3}$CrFeNiV, and AlCrFeNiV.

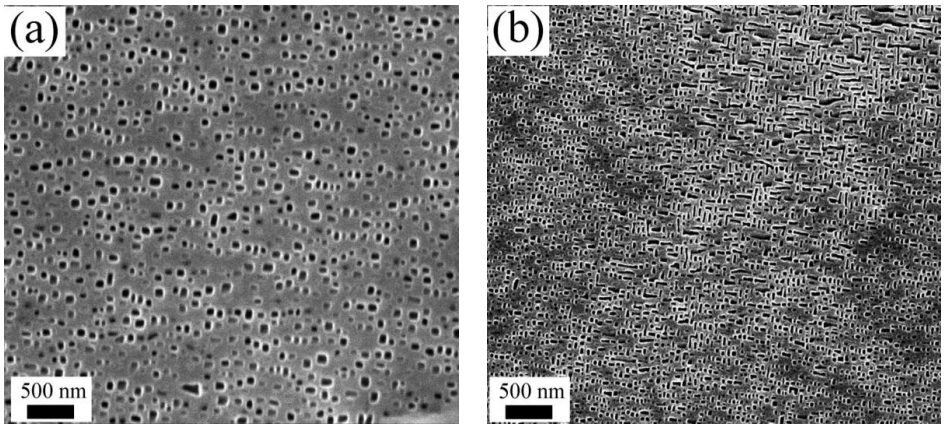

Figure 2. Back-scattering SEM images of: (**a**) $Al_{0.3}$CrFeNiV HEAs; and (**b**) $Al_{0.5}$CrFeNiV HEAs.

3.2. Results of the TEM and STEM

Figure 3a,b shows the bright field (BF) and STEM images of the $Al_{0.3}$CrFeNiV. Also, the corresponding selected area electron diffraction (SAED) pattern is presented in the inset of Figure 3a. It can be observed in the figures that a large number of spherical precipitates, with average diameters of approximately 100 nm, were distributed throughout the matrix. The SAED patterns suggested that the precipitates were a B2 phase, and the matrix was an A2 phase, as illustrated in Figure 3a. Figure 3b shows the STEM image of the $Al_{0.3}$CrFeNiV, and a clearer duplex phase structure can be clearly observed, which agreed with the results of the XRD and SEM.

In addition, the chemical compositions of the five different regions were measured by TEM-EDX. The average chemical compositions of the A2 and B2 phases in the $Al_{0.3}$CrFeNiV alloy are presented in Figure 3c. The TEM-EDX line scanning across a grain with a B2 structure was a representative region, which is marked in Figure 3b. The TEM-EDX results showed that the A2 phase was enriched in Fe, Cr, and V, while the B2 phase was enriched in Al and Ni. Therefore, based on the results of the TEM-EDX and the representative binary B2 intermetallic compounds AB (such as FeAl and NiAl) [17], it was expected that, for the B2 phase in the $Al_{0.3}$CrFeNiV, the Al atoms preferentially occupied the center sites of the unit cell where the A1 could be replaced by V since the V had a closer atomic radius to the Al. Meanwhile, the Ni and Fe randomly occupied the corner sites, and formed a (Ni, Fe) (Al, V) B2 structure similar to the NiAl due to the strongly negative formation enthalpy of the Al-Ni and V-Ni.

In regard to the $Al_{0.5}$CrFeNiV alloy, a representative TEM image is shown in Figure 4, and the corresponding SAED pattern is presented in the inset of Figure 4a. The red circles in the SAED pattern are the unidentified diffraction spots which suggested that, along with the coherent A2/B2 phases, another phase appeared in the alloy. The crystal structure of the phase was not identified in the current study. The STEM image of the $Al_{0.5}$CrFeNiV alloy is shown in Figure 4b. Two findings were observed in this study: (1) numerous spherical precipitates (the blue square in the inset of Figure 4b) with unknown structures and average diameters of approximately 80 nm, were found to be distributed throughout the matrix; (2) the typical inter-weaved short rods aligned at approximately 90° angles (the red circle in the inset of Figure 4b). It should be noted that the smaller spherical nano-precipitates were not uniformly distributed in the matrix, and the coherent A2/B2 phase mixture was also a characteristic feature of the spinodal structure, which may have been formed by periodic composition modulations during the solidification [18].

Moreover, it was determined that the chemical compositions of the five different grains were almost identical, and a representative TEM-EDX line scanning across the nano-precipitates can be seen in Figure 4b. The results of the TEM-EDX is shown in Figure 4c, where the spherical Cr- and V- rich nano-precipitates are shown as being dispersedly distributed in the alloy. These results indicated that higher contents of Al can cause another phase formation in the $Al_{0.5}$CrFeNiV HEAs, namely an

unknown phase. This resulted in the crystal structure of the phase not being identified in the current study. Therefore, based on the results of the chemical compositions of the unknown phase, it was assumed that the unknown phase was enriched in Cr and V due to the content of Cr (30 at %) and V (50 at %), as shown in Figure 4c. Furthermore, the unknown phase observed by the STEM may have corresponded to the minor unidentified peaks at small 2θ angles, which appeared in the XRD plot for the $Al_{0.5}$CrFeNiV alloy, as shown in Figure 1a. For the B2 phase in $Al_{0.5}$CrFeNiV alloy, it may have been a (Ni, Fe) Al type B2 structure, which was similar to the NiAl.

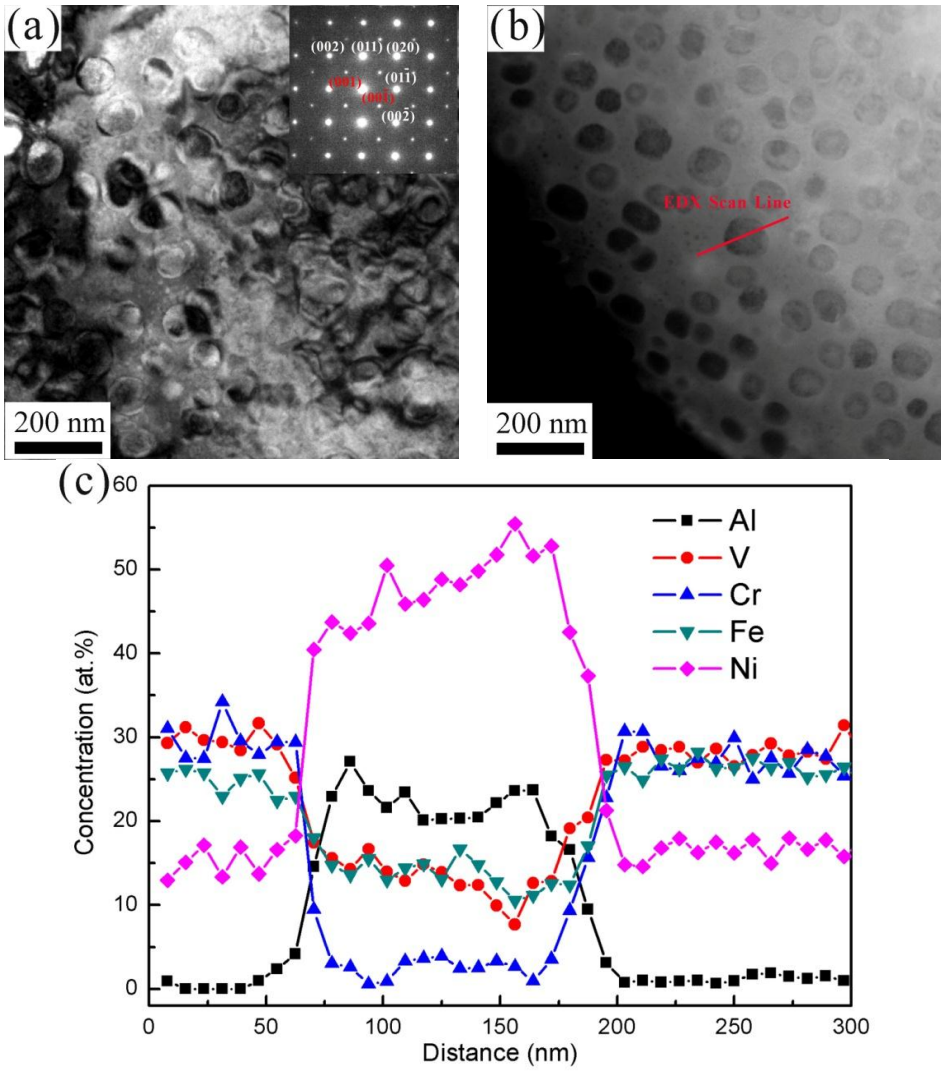

Figure 3. (**a**) BF TEM image of the $Al_{0.3}$CrFeNiV alloy and corresponding SAED patterns (zone axis [100]) showing the alloy consisted of a B2 phase, and an A2 phase; (**b**) STEM-HAADF image, where the red line indicates the EDX scan line; (**c**) Compositional profiles across the nano-precipitates.

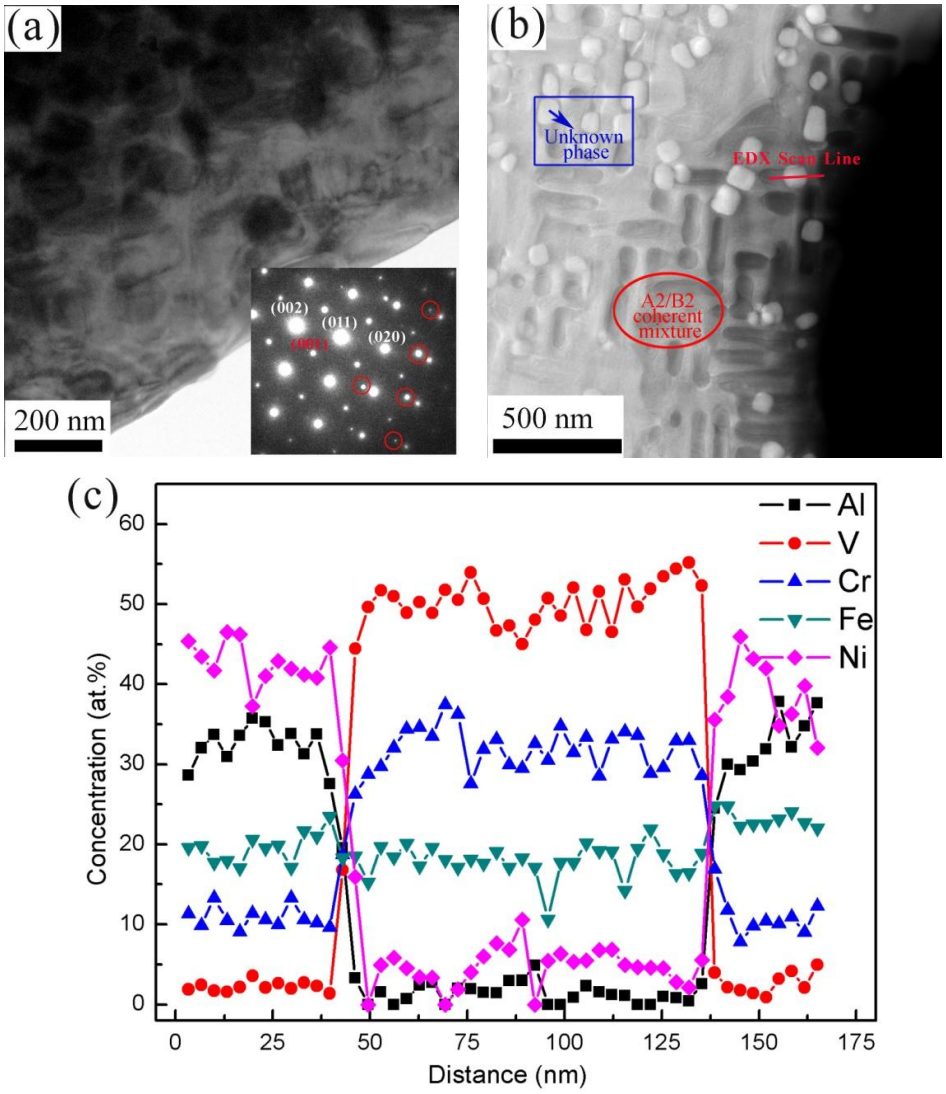

Figure 4. (**a**) BF TEM image of the $Al_{0.5}$CrFeNiV alloy and corresponding SAED patterns (zone axis [100]) showing the alloy consisted of a third phase, along with a B2 phase and an A2 phase; (**b**) STEM-HAADF image of the $Al_{0.5}$CrFeNiV alloy which clearly reveals the three different phases; (**c**) Compositional profiles across the unknown phase in the $Al_{0.5}$CrFeNiV alloys were found to be significantly enriched in Cr and V.

3.3. Mechanical Properties

Figure 5 shows the compression stress-strain curves of the Al_xCrFeNiV HEAs at the different Al content levels, and the values of the fracture strength (σ_b), yield strength ($\sigma_{0.2}$), and plastic strain limit (ε_p) are listed in Table 2. The two Al_xCrFeNiV alloys (x = 0.3 and x = 0.5) exhibited fairly high fracture strengths (>2700 MPa) and yield strengths (>2000 MPa). When x = 0.3, the fracture strength and plastic strain achieved the maximum levels, namely 3073 MPa and 9.2%, respectively. When the Al content was increased to x = 0.5, the yield strength was found to be increased, while the fracture strength and plastic strain limit decreased. It was interesting to note that the stress-strain curve of the $Al_{0.3}$CrFeNiV alloy exhibited a serration behavior, which was absent in the $Al_{0.5}$VCrFeNi. The observed serration behavior suggested that additional deformation mechanisms became active in $Al_{0.3}$CrFeNiV alloy, which may have been related to the formation of slip bands on the sample surfaces [10]. The serration behavior at room temperature presented a very interesting topic to be studied in regard to the HEAs, as it was observed at cryogenic temperatures [19], as well as elevated temperatures [20]. These findings may

potentially provide a new understanding of the mechanical-deformation behavior of HEAs at room temperature. Also, the results of more focused investigations will be reported in future publications. The comparisons which were completed with other typical HEAs and bulk metallic glasses (BMGs) are summarized in Table 2. It appeared that the $Al_{0.3}$CrFeNiV and $Al_{0.3}$CrFeNiV alloys had the desirable strength, but limited ductility among the listed materials. Moreover, the Young's modulus (E) could be calculated based on the true stress-strain curves (Figure 5b). The Young's moduli (E) of the $Al_{0.3}$CrFeNiV and $Al_{0.5}$CrFeNiV alloys were determined to be 113.5 GPa, and 111.8 GPa, respectively.

Table 2. Room temperature compression test results for the Al_xCrFeNiV (x = 0.3, and 0.5) HEAs compared with the other alloys from the material big-data.

No.	Alloy	$\sigma_{0.2}$ (MPa)	σ_p (MPa)	ε_p (%)	Ref.
1	$Al_{0.3}$CrFeNiV	2066.8	3072.8	9.2	This work
2	$Al_{0.5}$CrFeNiV	2295.7	2766.4	8.9	This work
3	$Al_{0.5}CrFeNiTi_{0.25}$	1880	3475	40	[21]
4	AlCoCrFeNi	1500	2830	26.9	[22]
5	$AlCoCrFeNiTi_{0.5}$	2260	3140	23.3	[22]
6	AlCoCrFeNiTi	1860	2580	8.8	[22]
7	CoCrCuFeNi	230	888	50.2	[23]
8	$CoCrCuFeNiTi_{0.5}$	700	1650	21.6	[23]
8	$CoCrCuFeNiTi_{0.8}$	1042	1848	2.11	[23]
10	CoCrCuFeNiTi	1227	1272	0	[23]
11	$Al_4Cu_{48}Zr_{48}$	1199	1882	5.3	[24]
12	$Al_{0.3}CoFeNiSi_{0.3}$	938	2857	33	[25]
13	MoNbTaW	1058	1211	1.5	[20]
14	MoNbTaVW	1246	1270	0.5	[20]
15	$CoCrFeMnNiV_{0.75}$	740	1325	7.8	[26]
16	CoCrFeMnNiV	1660	1845	0.5	[26]
17	AlNbTiV	1020	1318	5	[27]
18	AlCrCoCuFeNiV	1469	1970	16	[28]
19	AlCrCoCuFeNi	1303	2081	24	[28]
20	AlCrCoCuFeMnNi	1005	1480	15	[28]
21	AlCrCoCuFeNiTi	1234	1356	9	[28]

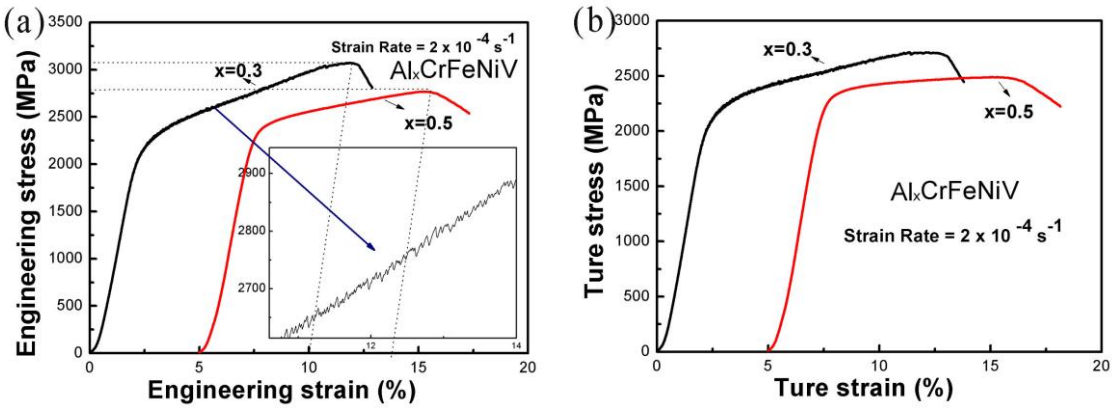

Figure 5. (**a**) Compressive engineering stress-strain curves; and (**b**) Compressive true stress-strain curves of the Al_xCrFeNiV HEAs (x = 0.3, and x = 0.5) cylindrical samples with 3 mm diameter × 6 mm height (with an aspect ratio of 2).

Figure 6 shows the morphologies of the fractographs of the Al_xCrFeNiV (x = 0.3, and x = 0.5) HEAs samples. Both of the fractographic morphologies of the two alloys exhibited typical river-like patterns and cleavage steps, which indicated that a cleavage fracture mechanism dominated the fracture process of both alloys. Furthermore, there were many microcracks observed (indicated by the

yellow arrows in the Figure 6) which prevailed on the cleavage fracture surface. These findings were consistent with the poor plasticity shown in Figure 5.

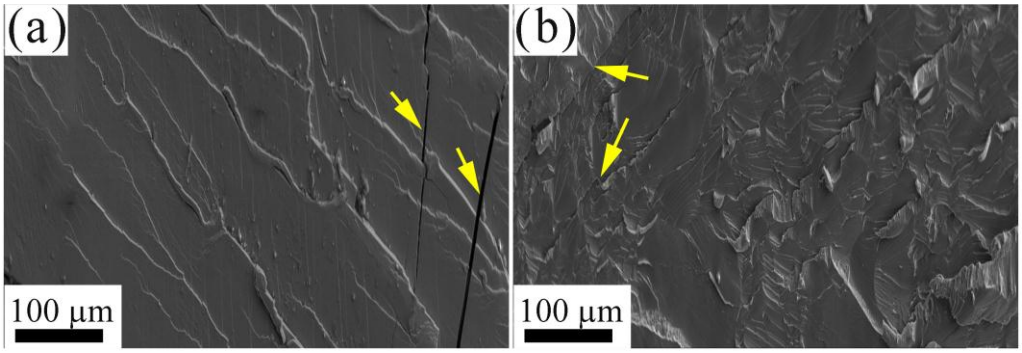

Figure 6. SEM images of fracture surfaces of: (**a**) $Al_{0.3}$CrFeNiV; and (**b**) $Al_{0.5}$CrFeNiV alloys following the compression deformation at room temperature; the yellow arrows indicate the microcracks.

In addition, the microhardness values of the as-cast Al_xCrFeNiV alloys (x = 0.3, 0.5, 0.75, 1, and 1.5) are given in Figure 7. The as-cast $Al_{0.3}$CrFeNiV alloy has a microhardness of 708 HV. The $Al_{0.5}$CrFeNiV alloy has a slightly lower microhardness of 680 HV. A further increase in the Al content results in a significant decrease first, then an increase in microhardness. For example, $Al_{0.75}$CrFeNiV has microhardness of 582 HV and $Al_{1.5}$CrFeNiV has microhardness of 694 HV. Combined with the result of the XRD (Figure 1a), it can be deduced that the volume fraction of unknown phase might affect the microhardness of Al_xCrFeNiV alloys due to the similar 'unknown phase' for $Al_{0.5}$CrFeNiV, $Al_{0.75}$CrFeNiV, and AlCrFeNiV alloys, respectively.

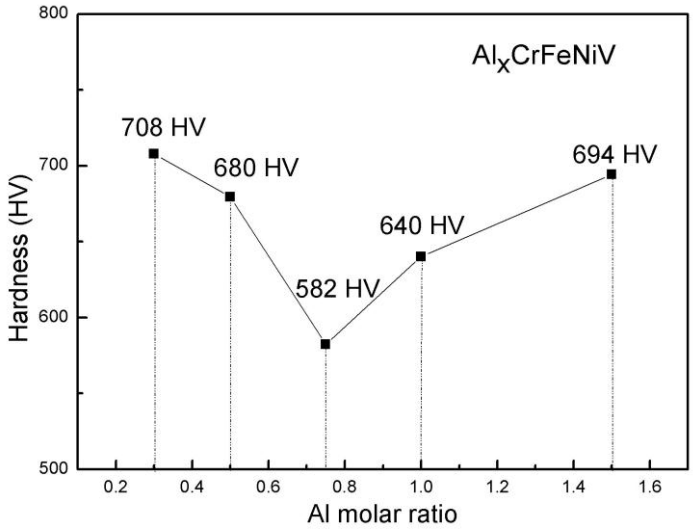

Figure 7. Dependence of microhardness of the as-cast Al_xCrFeNiV alloys on the Al molar ratio.

4. Discussion

In regard to the Co-Cr-Fe-Ni system HEAs, it has been proven that the addition of Al or V could promote the formation of an ordered phase. In particular, the effects of Al addition on the microstructure of the Al_xCoCrFeNi HEA system have been widely investigated [29–31]. It has been revealed that the microstructure of the Al_xCoCrFeNi HEAs evolved from a single A1, to A1 + B2, and B2 + A2 structures with increases in Al content [12]. Moreover, the alloying element V can also cause intermetallic phase formation in the CoCrFeMnNi and CoCrFeNi HEA systems [26].

In the present study, the alloy composition contained both V and Al elements, and thus the ordered phase was unavoidable. For the $Al_{0.3}$CrFeNiV alloy, it was observed that the alloy had typical duplex BCC structures, including A2 and B2 phases. Also, the B2 phase was enriched in Ni and Al, and the A2 matrix phase was enriched in V and Cr. When the Al content was increased to x = 0.5, the typical coherent A2/B2 phases and nano-precipitates could be observed. Otto et al. [8] investigated various factors which affect the phase stability of HEAs, and concluded that multiple phased microstructures, as well as intermetallic phases, would be formed when the enthalpy had greater influences than configurational entropy. Therefore, based on the viewpoints and results of the present study, it was expected that as the Al content increased, the Al and Ni elements would more easily be combined to form a B2 phase, due to the strongly negative formation enthalpy of B2 structure for Al-Ni [32]. When x = 0.5, along with the coherent A2/B2 phases, the unknown phases which contained large amounts of V and Cr were distributed in the alloy in the form of nano-precipitates.

In order to assist in analyzing the phase stability of the Al_xCrFeNiV alloys, certain derived thermodynamic parameters such as: δ (atomic size difference); ΔH_{mix} (enthalpy of mixing); Ω (ratio of entropy to enthalpy values); $\Delta\chi$ (Pauling electronegativity difference); and VEC (valence electron concentration) were calculated based on the following expressions [33]:

$$\delta = \sqrt{\sum_{i=1}^{n} c_i(1 - r_i/r)^2} \quad (1)$$

$$\Delta H_{mix} = \sum_{i=1, i\neq j}^{n} \Omega_{ij} c_i c_j \quad (2)$$

$$\Omega = \frac{T_m \Delta S_{mix}}{|\Delta H_{mix}|} \quad (3)$$

$$VEC = \sum_{i=1}^{n} c_i (VEC)_i \quad (4)$$

$$\Delta\chi = \sqrt{\sum_{i=1}^{n} c_i(\chi_i - \overline{\chi})^2} \quad (5)$$

where VEC is the average valence electron concentration; VEC_i is the valence electron concentration of element i; $\Delta\chi$ is the Pauling electronegativity difference; χ_i is the Pauling electronegativity of element i [34]; c_i, r_i, and χ_i are the atom fraction, radius, and electronegativity of the i-th element, respectively; and r_a and χ_a are the average radius and electronegativity of the elements in the alloys, respectively.

Table 3 presents the corresponding values of δ, ΔH_{mix}, ΔS_{mix}, T_{mix}, Ω, VEC, and $\Delta\chi$ for the Al_xCrFeNiV alloys (x = 0.3, and 0.5). It has been determined in previous studies that the small δ ($\leq$6.6%), near-zero values of the absolute ΔH_{mix} ($-$22 KJ/mol~5 KJ/mol), large values of Ω (~$\geq$1.1), and small $\Delta\chi$ (~$\leq$17.5%) effectively favor the formation of solid solutions, rather than that of intermetallic compounds. Also, the δ–ΔH_{mix}, δ–Ω, and δ–$\Delta\chi$ schemes could be adopted to predict the solid solution formations in HEAs [33,35,36]. Moreover, Guo et al. [37] concluded that the VEC could effectively predict the stability of BCC and FCC solid solutions in HEAs, and found that the BCC phase was stable at a lower VEC (<6.87). In this study, the values of the δ, ΔH_{mix}, ΔS_{mix}, Ω, and $\Delta\chi$ for the Al_xCrFeNiV alloys (x = 0.3, and 0.5) met the aforementioned criteria of the solid solution formations, which was found to be consistent with the experimental results. For example, the main phases of these HEAs were the disordered and ordered BCC solid solutions. On the other hand, the VEC values of the Al_xCrFeNiV alloys (x = 0.3, and 0.5) were determined to be very close to the critical values of the BCC solid solution formations, and thus the BCC phase was concluded to be in a stable state in this alloy system. In addition, comparing the properties of Co and V, it was found that the atomic radius of V element was larger than Co. Also, the heat of mixing (ΔH_{mix}) for V with other alloying elements was more negative than that of the Co with the same atomic pair. From these results, one could identify

that the Al_xCrFeNiV alloys with V alloying element effectively favored the formation of intermetallic phases, coinciding with the experimental results.

Table 3. Parameters of δ, ΔH_{mix}, ΔS_{mix}, T_m, Ω, *VEC*, and Δχ of the Al_xCrFeNiV (x = 0.3, and 0.5) alloys.

Alloys	δ (%)	ΔH_{mix} (kJ/mol)	ΔS_{mix} (J/mol·K)	T_m (K)	Ω	*VEC*	Δχ (%)
$Al_{0.3}$CrFeNiV	3.96	−11.83	12.83	1896.29	2.06	6.95	11.85
$Al_{0.5}$CrFeNiV	4.39	−13.14	13.15	1853.50	1.85	6.78	11.92

Generally, there is still additional work needed to study the five-component Al_xCrFeNiV HEAs, for example, annealing the samples to get equilibrium microstructure before the tests or comparing the difference in as-cast and annealed states may better reveal the microstructural evolutions in Al_xCrFeNiV alloys. However, in the present study, we mainly focused on the effects of the addition of Al on the crystal structures and mechanical properties of as-cast Al_xCrFeNiV HEAs. It should be sufficient to draw a conclusion that the increasing of Al in the B2 phase might cause the precipitate of the unknown phase in as-cast $Al_{0.5}$CrFeNiV alloy.

5. Conclusions

In the current research study, the five-component Al_xCrFeNiV (where x denotes the molar ratio, x = 0, 0.1, 0.3, 0.5, 0.75, 1, and 1.5) high-entropy alloys (HEAs) were prepared using an arc-melting furnace. The effects of the addition of the Al to the crystal structure were investigated using X-ray diffraction (XRD). Also, this study focused on the microstructures and mechanical properties of the two near-equiatomic HEAs, Al_xCrFeNiV (x = 0.3, and 0.5), and the following conclusions were made:

(1) The crystal structures of the alloys with lower Al content (for example, x = 0 and x = 0.1) were found to be quite different from the other Al contents. In contrast, distinctly similar crystal structures with BCC could be observed with a higher Al content (for example, $x \geq 0.3$);

(2) The $Al_{0.3}$CrFeNiV alloy was comprised of B2 and A2 phases. Meanwhile, the $Al_{0.5}$CrFeNiV alloy contained a third unknown phase, as well as the coherent A2/B2 phases. Furthermore, the unknown phase in the $Al_{0.5}$CrFeNiV alloy was found to be significantly enriched in Cr and V;

(3) Based on the mechanical properties tests, it was determined that both of the Al_xCrFeNiV (x = 0.3, and 0.5) alloys displayed very high yield and fracture strengths. However, they were very brittle, with compression fracture strains of less than 10%. Also, the as-cast $Al_{0.3}$CrFeNiV alloy has the highest microhardness of 708 HV among the as-cast Al_xCrFeNiV (x = 0.3, 0.5, 0.75, 1, and 1.5) HEAs. Therefore, efforts should be made to improve the ductility of these alloys. In addition, the fracture mechanisms of the Al_xCrFeNiV (x = 0.3, and 0.5) HEAs were determined to be cleavage fractures.

Acknowledgments: This research study was financially supported by the International Thermonuclear Experimental Reactor (ITER) 973 Program 2015GB113000 in China, as well as the National Natural Science Foundation of China (11335003, 91226202, 51471025). The authors would like to gratefully acknowledge the comments presented by Michael Gao.

Author Contributions: Yong Zhang conceived the idea of exploring novel high entropy alloys without Co-element. Songqin Xia carried out the microstructure and mechanical properties analysis of the Al_xCrFeNiV alloys. Xiao Yang, Mingbiao Chen, and Tengfei Yang prepared the alloy samples and also processed the analysis of the phase stability. All of the authors discussed the results and reviewed the manuscript.

Conflicts of Interest: The authors declare no conflict of interest.

References

1. Yeh, J.W.; Chen, S.K.; Lin, S.J.; Gan, J.Y.; Chin, T.S.; Shun, T.T.; Tsau, C.H.; Chang, S.Y. Nanostructured high-entropy alloys with multiple principal elements: novel alloy design concepts and outcomes. *Adv. Eng. Mater.* **2004**, *6*, 299–303. [CrossRef]

2. Zhang, Y.; Zuo, T.T.; Tang, Z.; Gao, M.C.; Dahmen, K.A.; Liaw, P.K.; Lu, Z.P. Microstructures and properties of high-entropy alloys. *Prog. Mater. Sci.* **2014**, *61*, 1–93. [CrossRef]
3. Gao, M.C.; Yeh, J.W.; Liaw, P.K.; Zhang, Y. *High-Entropy Alloys: Fundamentals and Applications*; Springer: Cham, Switzerland, 2016.
4. Lu, Z.P.; Wang, H.; Chen, M.W.; Baker, I.; Yeh, J.W.; Liu, C.T.; Nieh, T.G. An assessment on the future development of high-entropy alloys: Summary from a recent workshop. *Intermetallics* **2015**, *66*, 67–76. [CrossRef]
5. Wang, Y.P.; Li, B.S.; Fu, H.Z. Solid solution or intermetallics in a high-entropy alloy. *Adv. Eng. Mater.* **2009**, *11*, 641–644. [CrossRef]
6. Shaysultanov, D.G.; Stepanov, N.D.; Kuznetsov, A.V.; Salishchev, G.A.; Senkov, O.N. Phase composition and superplastic behavior of a wrought alcocrcufeni high-entropy alloy. *JOM* **2013**, *65*, 1815–1828. [CrossRef]
7. Singh, S.; Wanderka, N.; Murty, B.S.; Glatzel, U.; Banhart, J. Decomposition in multi-component AlCoCrCuFeNi high-entropy alloy. *Acta Mater.* **2011**, *59*, 182–190. [CrossRef]
8. Otto, F.; Yang, Y.; Bei, H.; George, E.P. Relative effects of enthalpy and entropy on the phase stability of equiatomic high-entropy alloys. *Acta Mater.* **2013**, *61*, 2628–2638. [CrossRef]
9. Yang, T.F.; Xia, S.Q.; Liu, S.; Wang, C.X.; Liu, S.S.; Zhang, Y.; Xue, J.M.; Yan, S.; Wang, Y.G. Effects of Al addition on microstructure and mechanical properties of Al_xCoCrFeNi high-entropy alloy. *Mater. Sci. Eng. A Struct.* **2015**, *648*, 15–22. [CrossRef]
10. Zhang, Y.; Qiao, J.W.; Liaw, P.K. A brief review of high entropy alloys serration behavior and flow units. *J. Iron Steel Res. Int.* **2016**, *23*, 2–6. [CrossRef]
11. Xia, S.Q.; Wang, Z.; Yang, T.F.; Zhang, Y. Irradiation behavior in high entropy alloys. *J. Iron Steel Res. Int.* **2015**, *22*, 879–884. [CrossRef]
12. Xia, S.Q.; Yang, X.; Yang, T.F.; Liu, S.; Zhang, Y. Irradiation resistance in Al_xCoCrFeNi high entropy alloys. *JOM* **2015**, *67*, 1–5. [CrossRef]
13. Wang, W.R.; Wang, W.L.; Wang, S.C.; Tsai, Y.C.; Lai, C.H.; Yeh, J.W. Effects of Al addition on the microstructure and mechanical property of Al_xCoCrFeNi high-entropy alloys. *Intermetallics* **2012**, *26*, 44–51. [CrossRef]
14. Jantzen, C.M.F.; Herman, H. Spinodal decomposition-phase diagram representation and occurrence. *Phase Diagr.* **1978**, 127–184.
15. Tong, C.J.; Chen, Y.L.; Chen, S.K.; Yeh, J.W.; Shun, T.T.; Tsau, C.H.; Lin, S.J.; Chang, S.Y. Microstructure characterization of Al_xCoCrCuFeNi high-entropy alloy system with multiprincipal elements. *Metall. Mater. Trans. A Phys. Metall. Mater. Sci.* **2005**, *36A*, 881–893. [CrossRef]
16. Hanna, J.A.; Baker, I.; Wittmann, M.W.; Munroe, P.R. A new high-strength spinodal alloy. *J. Mater. Res.* **2005**, *20*, 791–795. [CrossRef]
17. Pike, L.; Chang, Y.; Liu, C. Point defect concentrations and hardening in binary B2 intermetallics. *Acta Mater.* **1997**, *45*, 3709–3719. [CrossRef]
18. Santodonato, L.J.; Zhang, Y.; Feygenson, M.; Parish, C.M.; Gao, M.C.; Weber, R.J.K.; Neuefeind, J.C.; Tang, Z.; Liaw, P.K. Deviation from high-entropy configurations in the atomic distributions of a multi-principal-element alloy. *Nat. Commun.* **2015**, *6*, 1–13. [CrossRef] [PubMed]
19. Laktionova, M.A.; Tabchnikova, E.D.; Tang, Z.; Liaw, P.K. Mechanical properties of the high-entropy alloy $Al_{0.5}$CoCrCuFeNi at temperatures of 4.2–300 K. *Low Temp. Phys.* **2013**, *39*, 630–632. [CrossRef]
20. Senkov, O.N.; Wilks, G.B.; Scott, J.M.; Miracle, D.B. Mechanical properties of $Nb_{25}Mo_{25}Ta_{25}W_{25}$ and $V_{20}Nb_{20}Mo_{20}Ta_{20}W_{20}$ refractory high entropy alloys. *Intermetallics* **2011**, *19*, 698–706. [CrossRef]
21. Liu, S.; Gao, M.C.; Liaw, P.K.; Zhang, Y. Microstructures and mechanical properties of Al_xCrFeNi$Ti_{0.25}$. *J. Alloy. Compd.* **2015**, *619*, 610–615. [CrossRef]
22. Zhou, Y.J.; Zhang, Y.; Wang, Y.L.; Chen, G.L. Solid solution alloys of AlCoCrFeNiTi_x with excellent room-temperature mechanical properties. *Appl. Phys. Lett.* **2007**, *90*. [CrossRef]
23. Wang, X.F.; Zhang, Y.; Qiao, Y.; Chen, G.L. Novel microstructure and properties of multicomponent CoCrCuFeNiTi_x alloys. *Intermetallics* **2007**, *15*, 357–362. [CrossRef]
24. Chen, J.; Zhang, Y.; He, J.; Yao, K.; Wei, B.; Chen, G. Metallographic analysis of Cu-Zr-Al bulk amorphous alloys with yttrium addition. *Scr. Mater.* **2006**, *54*, 1351–1355. [CrossRef]
25. Zhang, Y.; Zuo, T.T.; Cheng, Y.Q.; Liaw, P.K. High-entropy alloys with high saturation magnetization, electrical resistivity, and malleability. *Sci. Rep.* **2013**, *3*, 1335–1338. [CrossRef] [PubMed]

26. Stepanov, N.D.; Shaysultanov, D.G.; Salishchev, G.A.; Tikhonovsky, M.A.; Oleynik, E.E.; Tortika, A.S.; Senkov, O.N. Effect of V content on microstructure and mechanical properties of the CoCrFeMnNiV$_x$ high entropy alloys. *J. Alloy. Compd.* **2015**, *628*, 170–185. [CrossRef]
27. Stepanov, N.D.; Shaysultanov, D.G.; Salishchev, G.A.; Tikhonovsky, M.A. Structure and mechanical properties of a light-weight AlNbTiV high entropy alloy. *Mater. Lett.* **2015**, *142*, 153–155. [CrossRef]
28. Li, B.S.; Wang, Y.P.; Ren, M.X.; Yang, C.; Fu, H.Z. Effects of Mn, Ti and V on the microstructure and properties of AlCrFeCoNiCu high entropy alloy. *Mater. Sci. Eng. A* **2008**, *498*, 482–486. [CrossRef]
29. Li, C.; Li, J.C.; Zhao, M.; Jiang, Q. Effect of aluminum contents on microstructure and properties of Al$_x$CoCrFeNi alloys. *J. Alloy. Compd.* **2010**, *504S*, S515–S518. [CrossRef]
30. Manzoni, A.; Daoud, H.; VÖlkl, R.; Glatzel, U.; Wanderka, N. Phase separation in equiatomic AlCoCrFeNi high-entropy alloy. *Ultramicroscopy* **2013**, *132*, 212–215. [CrossRef] [PubMed]
31. Chou, H.P.; Chang, Y.S.; Chen, S.K.; Yeh, J.W. Microstructure, thermophysical and electrical properties in Al$_x$CoCrFeNi ($0 \leq x \leq 2$) high-entropy alloys. *Mater. Sci. Eng. B Solid* **2009**, *163*, 184–189. [CrossRef]
32. Li, C.; Zhao, M.; Li, J.C.; Jiang, Q. B2 structure of high-entropy alloys with addition of Al. *J. Appl. Phys.* **2008**, *104*, 113504. [CrossRef]
33. Yang, X.; Chen, S.Y.; Cotton, J.D.; Zhang, Y. Phase Stability of Low-Density, Multiprincipal Component Alloys Containing Aluminum, Magnesium, and Lithium. *JOM* **2014**, *66*, 2009–2020. [CrossRef]
34. Dong, Y.; Lu, Y.; Jiang, L.; Wang, T.; Li, T. Effects of electro-negativity on the stability of topologically close-packed phase in high entropy alloys. *Intermetallics* **2014**, *52*, 105–109. [CrossRef]
35. Yang, X.; Zhang, Y. Prediction of high-entropy stabilized solid-solution in multi-component alloys. *Mater. Chem. Phys.* **2012**, *132*, 233–238. [CrossRef]
36. Fang, S.; Xiao, X.; Xia, L.; Li, W.; Dong, Y. Relationship between the widths of supercooled liquid regions and bond parameters of Mg-based bulk metallic glasses. *J. Non-Cryst. Solids.* **2003**, *321*, 120–125. [CrossRef]
37. Guo, S.; Ng, C.; Lu, J.; Liu, C.T. Effect of valence electron concentration on stability of FCC or bcc phase in high entropy alloys. *J. Appl. Phys.* **2011**, *109*, 645–647. [CrossRef]

© 2017 by the authors; licensee MDPI, Basel, Switzerland. This article is an open access article distributed under the terms and conditions of the Creative Commons Attribution (CC-BY) license (http://creativecommons.org/licenses/by/4.0/).